Okhotsk Sea and Polar Oceans Research 5 (2021) 31-35

Article

Large-Scale Sea Ice Divergence and Convergence Monitoring in the Arctic Ocean during Spring 2018

Mariapina VOMERO[1], Noriaki KIMURA[2], Mathias MILZ[3], Victoria BARABASH[3] and Hajime YAMAGUCHI[1]

[1] *Graduate School of Frontier Sciences, The University of Tokyo, Kashiwa, Japan*
[2] *Atmosphere and Ocean Research Institute, The University of Tokyo, Kashiwa, Japan*
[3] *Department of Computer Science, Electrical and Space Engineering, Luleå University of Technology, Kiruna, Sweden*

(Received November 2, 2020; Revised manuscript accepted January 23, 2021)

Abstract

This study investigates sea ice motion in the Arctic Ocean during the year 2018 to detect areas of ice deformation. We aim to improve the current understanding of large-scale sea ice circulation by examining ice convergence/divergence during the early melt-season. OSISAF sea ice drift data provided by EUMETSAT were used for the analysis during the months of March and April. Daily ice drifting speed and deformation parameters showed a strong correlation throughout the observed interval, while a local-scale analysis revealed different patterns for ice divergence and convergence in areas of enhanced ice drift.

Key words: sea ice drift, Arctic Ocean, OSISAF, remote sensing, ice divergence

1. Introduction

Monitoring allowed by current remote sensing systems with multi-sensor sources has led to improved analysis and a more detailed understanding of sea ice motion. Several studies investigated the variability of sea ice divergence in different regions of the Arctic from satellite records. Frey and others (2015) observed significant changes in sea ice cover across the Bering, Chukchi, and Beaufort seas of the Pacific Arctic Region. The patterns revealed were spatially heterogeneous, with significant declines in ice extent over the Chukchi and Beaufort seas. Their results suggested that some areas are experiencing rapid shifts in sea ice cover due to different drivers, being primarily wind driven in the Beaufort Sea, thermally driven in the Canada Basin, and influenced by both in the Bering Sea.

Kimura and others (2013) identified potential relationships between interannual difference in winter ice motion and ice area in the following summer using ice velocity data with a 37.5 km grid resolution from the satellite passive microwave sensor Advanced Microwave Scanning Radiometer (AMSR). Using a large-scale approach, they tracked sea ice deformation for the seasonal ice cover, which is now the dominant ice type in the Arctic. From their analysis of sea ice divergence and convergence, it was observed that the winter ice redistribution controls spring ice thickness until summer.

Kwok (2015) defined a method to study the converging motion along the Arctic coasts of Greenland and the Canadian Arctic Archipelago using satellite data for ice drift from the Special Sensor Microwave Imager (SSMI) and Advanced Scatterometer (ASCAT) data. Convergence patterns were identified along the coastal boundaries of the Arctic Basin, where pressure ridges and thicker ice are formed from the shear motion of ice floes in close contact. The ice resulting from these processes is more likely to accumulate on the multiyear ice and survive the summer months, consequentially slowing down the decline of sea ice coverage. The redistribution of the ice cover also intensifies local ice growth with resulting increased ice strength and roughness that alters the mechanical response to atmospheric and oceanic drivers.

The aim of this study is to identify both the divergence and convergence of ice motion in the Arctic Ocean during the early melt-season and to describe large-scale sea ice deformation processes during spring 2018 (60 days in total). Investigating differences in these deformation mechanisms is useful to establish an improved representation of sea ice motion for modeling studies. Spatial and temporal patterns in dispersion processes are addressed at both the periphery and interior of the ice pack to provide a global description over the whole Arctic Ocean. For this reason, the Ocean and Sea Ice Satellite Application

Facility (OSISAF) ice drift data, provided by the European Organization for the Exploitation of Meteorological Satellites (EUMETSAT), were chosen to guarantee a complete spatial coverage since it is based on low resolution (10 - 15 km) Passive Microwave instruments such as AMSR-2.

2. Data

The OSISAF low resolution ice drift dataset is daily computed from aggregated maps of passive microwave (e.g. SSMI, AMSR-2) or scatterometer (e.g. ASCAT) signals. Each map can be either derived from one sensor used as input to the processing chain (single sensor product) or from a merged (multi-sensor) dataset. Its characteristic wide ground swaths, high acquisition rates and all-weather capability ensure daily monitoring of both polar regions based on global ice drift vectors with a spatial resolution of 62.5 km.

Since these data were processed from a pair of satellite images after implementing the Continuous Maximum Cross Correlation algorithm (Lavergne and others 2010), the resulting ice drift vector describes the displacement that each ice cell observed at the initial position (lat_0, lon_0) shows at the position (lat_1, lon_1) after 48 hours. This temporal resolution limits the application of such imagery for highly variable drift speeds close to the ice edge or the coast (Williams and others, 2019), therefore these pixels were excluded from the analysis. Furthermore, due to the limited accuracy of data from summer months (defined as the period from April 30th to October 1st for the Northern Hemisphere) caused by atmospheric noise and ice surface melting (Peterson and Stanton, 2016), the present paper will only address the early melt season during the months of March and April.

3. Observation Method and Result

The deformation metrics of sea ice divergence and convergence enables the description of closure and opening processes of the ice pack. This ice deformation parameter is defined by the following equation (Tabata and others, 1980):

$$(1)\quad \dot{\nabla} = \frac{\partial u}{\partial x} + \frac{\partial v}{\partial y} = u_x + v_y$$

where u(x,y) and v(x,y) are the drift components in x- and y-direction at position (x,y). The dimension of $\dot{\nabla}$is velocity change per length unit, hence $[time]^{-1}$.

Kimura and Wakatsuchi (2004) calculated the partial derivatives of the drift vector field at a generic cell (i, j) as a rate of spatial change around the boundaries of a grid cell instead of the derivatives of the velocities as follows:

$$(2)\quad \dot{\nabla}_{i,j} = \frac{u\left(i+\frac{1}{2},j\right)-u\left(i-\frac{1}{2},j\right)}{dist} + \frac{v\left(i,j+\frac{1}{2}\right)-v\left(i,j-\frac{1}{2}\right)}{dist}$$

where *dist* is the grid resolution (62.5 km).
This formula was applied to the spatial gradients of ice motion computed from OSISAF dataset. Depending on the sign of the sum $u_x + v_y$, the final parameter is classified as divergence or convergence. As a measure of area change, a negative divergence (now defined as convergence) at a specific point indicates a converging vector field at that point, while positive values allow to identify where a diverging vector field potentially originates from. Therefore, the evaluation of ice divergence highlights characteristics not easily noticeable when using ice motion vectors only.

Daily mean values for sea ice drift, divergence and convergence were computed from OSISAF ice drift fields over 48 hours (Fig.1). Since ice convergence corresponds to negative divergence, it was plotted in Fig.1 as absolute values for comparison to positive divergence values.

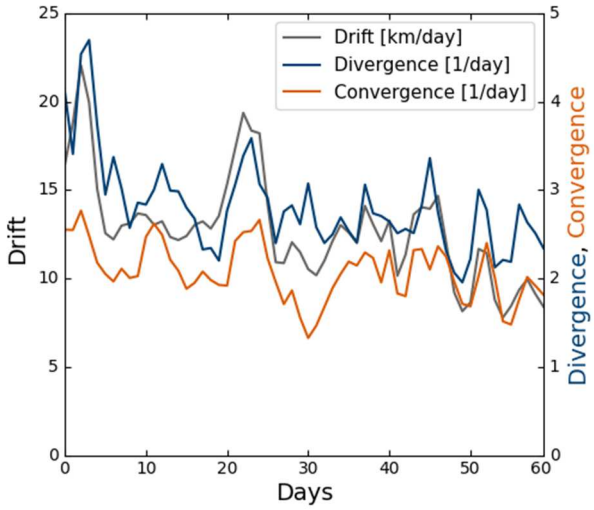

Fig. 1 Trends of sea ice drift, divergence and convergence during Spring (March – April) 2018

In order to quantify the similarity between ice drift and the other parameters, the Pearson correlation coefficient was computed using the following formula for n samples of two generic variables x and y:

$$(3)\quad \rho_{xy} = \frac{\sum_{i=1}^{n}(x_i-\bar{x})(y_i-\bar{y})}{\sqrt{\sum_{i=1}^{n}(x_i-\bar{x})^2}\sqrt{\sum_{i=1}^{n}(y_i-\bar{y})^2}}$$

Results for spring 2018 are displayed in Fig.2 and 3.

Both coefficients of about 0.78 showed a strong temporal correlation for both convergence and divergence to the ice drift trend. However, a spatial analysis allows to describe regional patterns for these deformation parameters. Therefore, vector field maps

of the Arctic Ocean were created to depict their interplay during the observed interval.

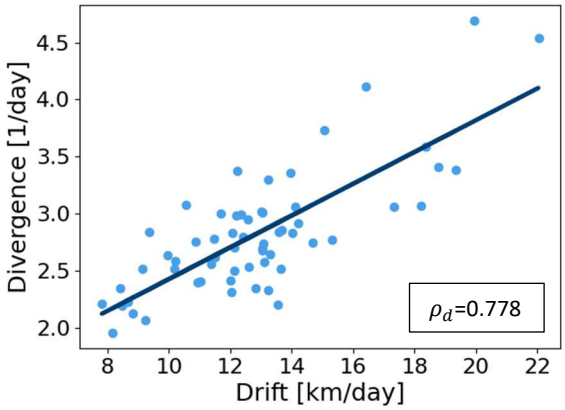

Fig. 2 Drift and Divergence scatter plot and correlation coefficient - Spring 2018

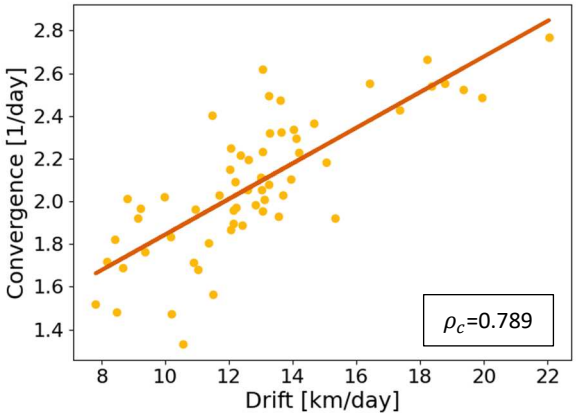

Fig. 3 Drift and Convergence scatter plot and correlation coefficient - Spring 2018

The sea-ice drift map for spring 2018 (Fig. 4) shows two distinct features: an anticyclonic motion in the Canadian basin, i.e. the Beaufort Gyre , and the Transpolar drift that drives the ice from the Laptev Sea across the Pole to the Fram Strait (Rigor and Wallace, 2004). In addition to these two dominant Arctic circulation patterns, a motion system was also identified from the Kara to the Barents Sea. The corresponding values in these areas exceeded 20 km/day.

The frequency map of intense ice motion in Fig. 5 was computed from pixels corresponding to a value higher than 10 km/day (chosen according to the study on strong drift patterns performed by Kaur and others, 2015) in order to identify areas of persistent strong sea ice speeds. This graph emphasizes the high correspondence between previously detected areas of intense and recurrent drift motion regimes. In fact, strong sea ice motion was detected in the Greenland and the Barents Seas for almost the entire length of this study.

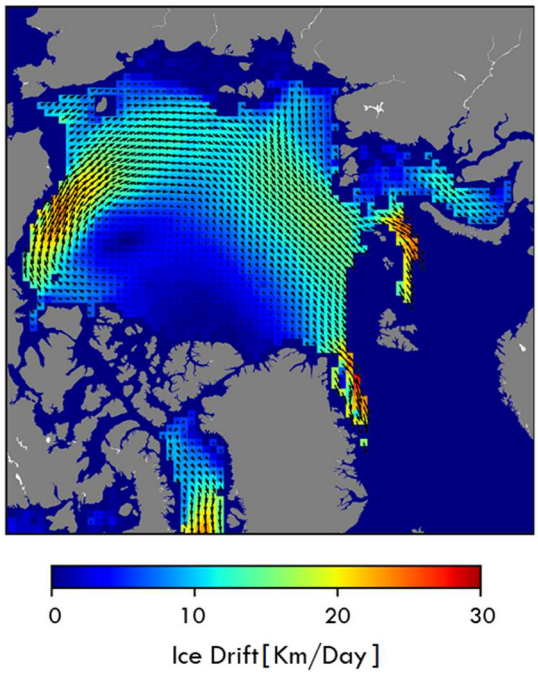

Fig. 4 Sea ice drift speed and vector map averaged for the observed interval (March - April, 2018)

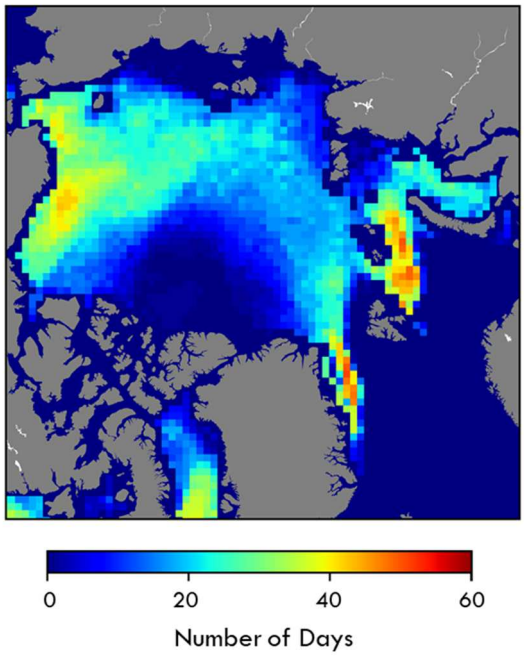

Fig. 5 Frequency map of strong ice motion for Spring 2018

The relationship between sea ice drift and divergence was further examined to identify areas for

sea ice deformation. A strong diverging pattern was identified in Fig.7 after setting a threshold to the most recurrent value of ice divergence grid cells during the observed interval (equal to 3 from the histogram in Fig. 6).

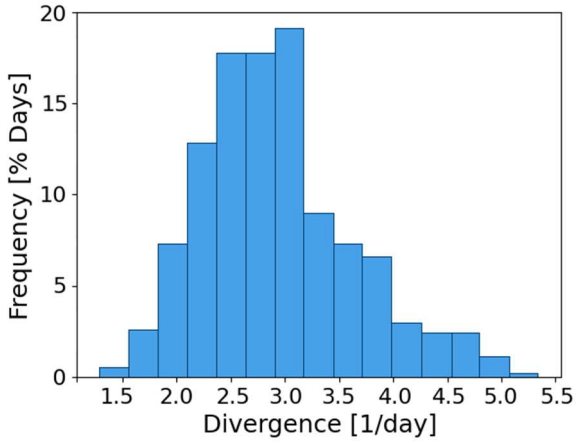

Fig. 6 Histogram of ice divergence during Spring 2018

Figure 7 shows that most of the divergent cells are located in offshore sites of the Chukchi, Laptev and East Siberian Seas. When comparing these results with the previous sea ice drift frequency map (Fig.5), areas of intense sea ice motion only overlap in the Chukchi Sea which is linked to the change in the relative strength and location of the Beaufort Gyre versus the Transpolar Drift (De Vernal *and others*, 2005).

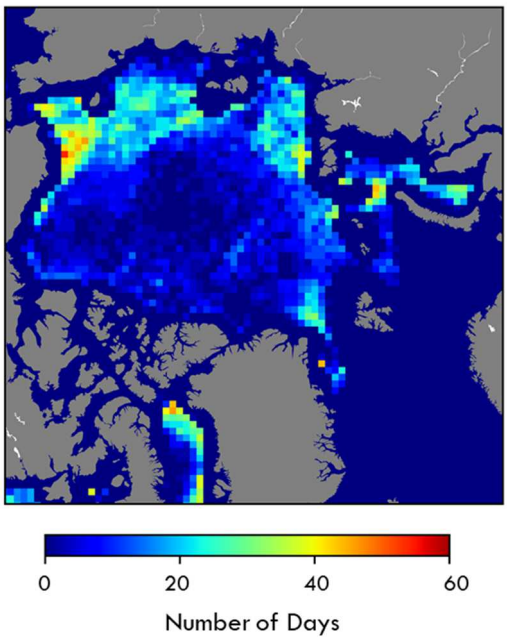

Fig. 7 Frequency map of persistent divergence - Spring 2018

Therefore, the remaining areas of strong ice motion detected in Fig.5 aren't linked to dispersing mechanisms exclusively. Values of persistent convergence (threshold set at 2 from Fig.8 for convergence grid cells) were found in the Beaufort, Kara and Greenland Seas as charted in Fig. 9.

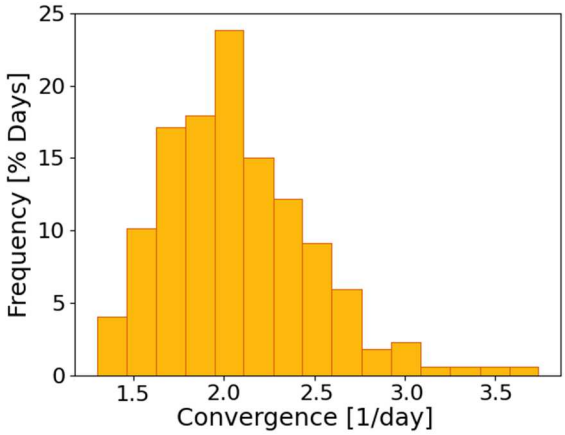

Fig. 8 Histogram of ice convergence during Spring 2018

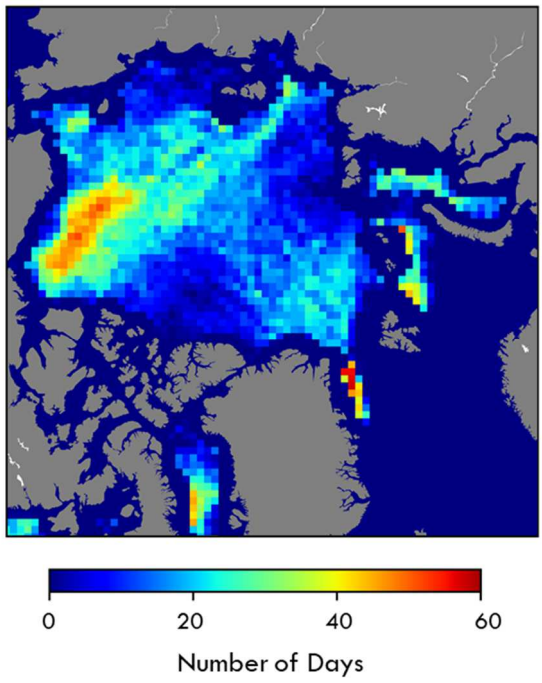

Fig. 9 Frequency map of persistent convergence - Spring 2018

This higher level of correspondence between convergence and ice-drifting speed is particularly enhanced in the Beaufort Sea, where the anticyclonic (clockwise) circulation of the Beaufort Gyre intensifies sea ice concentrations and ice ridging phenomena (Asplin and others, 2009). Off the coasts of Greenland

ice convergence is attributable to the onshore ice circulation depicted in Fig. 9 (Kwok, 2015). Lastly, the sea ice transport into the Barents Sea directed towards the Norwegian Seas represents the third noticeable area where correlation with intense convergence takes place.

4. Conclusions

In this study, three parameters for sea ice deformation were mapped over the Arctic Ocean using OSISAF data for spring 2018. The global analysis showed a noticeable correlation between the temporal change of sea ice drift and diverging/converging trends. From the analysis of the ice drift dataset, areas of strong drift patterns also confirmed the influence of the two main wind-driven ocean currents of the Beaufort Gyre and the Transpolar Drift Stream.

Values of divergence and convergence were further investigated to provide insight into the nature of motion in different areas of the Arctic sea. During the time interval considered in this paper both indicators overall showed a high correlation to intense ice drift values. Remarkable converging motion was observed in the Greenland and Barents Sea, while high diverging movements in the Chukchi Sea. Furthermore, consistent and persistent ice motion induced a widespread convergence in the Beaufort Sea.

Acknowledgments

The authors express their sincere gratitude to OSISAF and its data provider. This work was also supported by the Arctic Challenge for Sustainability (ArCS) project in Japan.

References

Asplin, M. G., J. V. Lukovich, and D. G. Barber (2009). Atmospheric forcing of the Beaufort Sea ice gyre: Surface pressure climatology and sea ice motion. *Journal of Geophysical Research: Oceans,* **114** (C1).

De Vernal A., C. M. Hillaire, and D. A. Darby (2005). Variability of sea ice cover in the Chukchi Sea (western Arctic Ocean) during the Holocene. *Paleoceanography,* **20** (4). https://doi.org/10.1029/2005PA001157

Frey, K. E., G. W. K. Moore, L. W. Cooper, and J. M. Grebmeier (2015). Divergent patterns of recent sea ice cover across the Bering, Chukchi, and Beaufort seas of the Pacific Arctic Region. *Progress in Oceanography*, **136**, 32-49.

Kaur, S., J. K. Ehn, and D. G. Barber (2018). Pan-arctic winter drift speeds and changing patterns of sea ice motion: 1979–2015. *The Polar Record,* **54** (5-6), 303-311.

Kimura, N., and M. Wakatsuchi (2004). Increase and decrease of sea ice area in the Sea of Okhotsk: Ice production in coastal polynyas and dynamic thickening in convergence zones. *Journal of Geophysical Research: Oceans*, **109** (C9).

Kimura, N., A. Nishimura, Y. Tanaka, and H. Yamaguchi (2013). Influence of winter sea-ice motion on summer ice cover in the Arctic. *Polar Research*, **32** (1), 20193.

Kwok, R. (2015). Sea ice convergence along the Arctic coasts of Greenland and the Canadian Arctic Archipelago: Variability and extremes (1992–2014). *Geophysical Research Letters*, **42** (18), 7598-7605.

Lavergne, T., S. Eastwood, Z. Teffah, H. Schyberg, and L. A. Breivik (2010). Sea ice motion from low-resolution satellite sensors: An alternative method and its validation in the Arctic. *Journal of Geophysical Research: Oceans*, **115** (C10).

Peterson, E. R., and T. P. Stanton (2016). Comparing the Accuracy of AMSRE, AMSR2, SSMI and SSMIS Satellite Radiometer Ice Concentration Products with One-Meter Resolution Visible Imagery in the Arctic. *AGUFM*, 2016, C13C-0849.

Rigor, I. G., and J. M. Wallace (2004). Variations in the age of Arctic sea‐ice and summer sea‐ice extent. *Geophysical Research Letters* **31** (9).

Tabata, T., T. Kawamura and M. Aota (1980). Divergence and rotation of an ice field off Okhotsk Sea Coast of Hokkaido. Sea Ice Processes and Models (RS Pritchard, Ed.), University of Washington Press, Seattle, Washington, 98195.

Williams, T., A. Korosov, P. Rampal and E. Ólason (2019). Presentation and evaluation of the Arctic sea ice forecasting system neXtSIM-F. *Cryosphere*. https://doi.org/10.5194/tc-2019-154

Correspondence to: M. Vomero,
mariapina.vomero@gmail.com